Chemical Science

ROYAL SOCIETY OF CHEMISTRY

EDGE ARTICLE

View Article Online
View Journal | View Issue

Check for updates

Cite this: *Chem. Sci.*, 2022, **13**, 5305

All publication charges for this article have been paid for by the Royal Society of Chemistry

Rational design of a promising oxychalcogenide infrared nonlinear optical crystal†

Yansong Cheng, Hongping Wu, Hongwei Yu,* Zhanggui Hu, Jiyang Wang and Yicheng Wu

Received 6th January 2022
Accepted 11th April 2022

DOI: 10.1039/d2sc00099g

rsc.li/chemical-science

Oxychalcogenides with the performance-advantages of both chalcogenides and oxides are emerging materials class for infrared (IR) nonlinear optical (NLO) crystals that can expand the wavelength of solid-state lasers to IR regions and are of importance in industrial and civil applications. But rationally designing a high-performance oxychalcogenide NLO crystal remains a great challenge. Herein, we chose the melilite-type $Sr_2ZnSi_2O_7$ as the structure template. Through part isovalent substitution of S^{2-} for O^{2-} anions, the first hetero-anionic thiostannate $Sr_2ZnSn_2OS_6$ with wide IR transmission has been synthesized. More importantly, compared to the maternal oxide, $Sr_2ZnSi_2O_7$, the second harmonic generation (SHG) response of $Sr_2ZnSn_2OS_6$ is enhanced by two orders of magnitude. In addition, $Sr_2ZnSn_2OS_6$ can exhibit a large band-gap and high laser damage threshold. These advantages make $Sr_2ZnSn_2OS_6$ a promising IR NLO crystal. Our research will provide insights into the rational design of new IR NLO crystals.

Introduction

Mid-infrared (MIR) sources covering 3 to 5 μm and 8 to 12 μm are of great interest in industrial and civil applications such as molecular spectroscopy, remote sensing, free-space communication, and environmental monitoring.[1–5] However, it is difficult for solid-state lasers to directly radiate MIR coherent light. Nevertheless, relying on frequency conversion techniques of nonlinear optical (NLO) crystals, such as optical parametric oscillators (OPOs) and optical parametric amplifiers (OPAs), is an effective way for solid-state lasers to generate MIR radiation. In these processes, the performances of NLO crystals determine the conversion efficiency of IR coherent light. So, they play a strategically important role in the development of IR lasers. In the past three decades, although a series of high-performance NLO crystals have been discovered and widely commercialized in the ultraviolet and visible regions, including β-BaB_2O_4 (BBO),[6] LiB_3O_5 (LBO),[7] $CsLiB_6O_{10}$ (CLBO),[8] KH_2PO_4 (KDP)[9] and $KTiOPO_4$ (KTP),[10] NLO crystals available in the infrared (IR) region are still seldom, and they are mainly some chalcopyrite-type chalcogenides, such as $AgGaQ_2$ (Q = S, Se)[11,12] and $ZnGeP_2$.[13] Although these crystals feature very large second harmonic generation (SHG) coefficients, the low laser damage thresholds (LDTs) of $AgGaQ_2$ (Q = S, Se) and harmful two-photon absorption (TPA) of $ZnGeP_2$ limit their wide applications,[14] particularly under high-power conditions. So, exploring new IR NLO crystals with high LDTs and large band gaps is still a current research interest.[15–18]

For the design of new IR NLO crystals, metal chalcogenides, oxides and halides are the three most important materials. Regarding chalcogenides, they generally exhibit large SHG responses and wide IR transparency,[19,20] while low LDTs and undesired TPA caused by their small band-gaps as well as the difficulty in crystal growth are the main problems restricting their wide applications, just as observed in typical $AgGaQ_2$ (Q = S, Se) and $ZnGeP_2$.[21] Compared to chalcogenides, metal oxides can exhibit larger band-gaps and thus higher LDTs as well as easier crystal growth.[22] But the poor IR transparency and relatively weak SHG responses make their application limited within 5 μm.[23] Therefore, it is clear that chalcogenides can exhibit larger SHG response and better IR transmission, while metal oxides have advantages in band-gaps and LDTs. Therefore, combining two types of anions may be an expectant strategy for designing high-performance IR NLO crystals with balanced properties. Up to now, although some oxychalcogenide IR NLO crystals, *e.g.* $SrZn_2OS_2$ (E_g = 3.86 eV, 0.06× $AgGaS_2$),[24] $Sr_5Ga_8O_3S_{14}$ (E_g = 3.90 eV, 0.8× $AgGaS_2$),[25] $SrGeOSe_2$ (E_g = 3.16 eV, 1.3× $AgGaS_2$),[26] $BaGeOSe_2$ (E_g = 3.20 eV, 1.1× $AgGaS_2$),[27] and $Sr_6Cd_2Sb_6O_7S_{10}$ (E_g = 1.89 eV, 4.0× $AgGaS_2$),[28] have been reported, these compounds are still less investigated than their maternal oxides or chalcogenides. In particular, how to optimize the structure of oxychalcogenides to use the advantages of oxides and chalcogenides to the maximum through a rational structure design is still indistinct.

Tianjin Key Laboratory of Functional Crystal Materials, Institute of Functional Crystal, Tianjin University of Technology, Tianjin 300384, China. E-mail: hwyu15@gmail.com

† Electronic supplementary information (ESI) available. CCDC 2132019. For ESI and crystallographic data in CIF or other electronic format see **https://doi.org/10.1039/d2sc00099g**

In this research, we choose the melilite-type $Sr_2ZnSi_2O_7$ as a structural template to design a new oxychalcogenide through rational chemical substitution. $Sr_2ZnSi_2O_7$[29] crystallizes in the noncentrosymmetric (NCS) space group $P\bar{4}2_1m$. Its structure features a pentagon-like layer, which endows its structure with better flexibility and designability. But remarkably, the SHG response of $Sr_2ZnSi_2O_7$ is only 35.0× α-SiO_2,[30] almost two orders of magnitude smaller than that of $AgGaS_2$. And owing to the absorption of the metal–oxygen bonds, it also has poor IR transmission. In our study, we used Sn atoms to substitute Si in melilite-type $Sr_2ZnSi_2O_7$, first, because Sn atoms are heavier and more polarizable than Si atoms, which is helpful for the material to exhibit a wider IR transmission and larger SHG response.[31] Furthermore, with the help of the unique pentagonal layer configurations, we expect to use heavier and more polarizable S atoms to selectively substitute the terminal O atoms in the pentagonal layers as well as the bridging O atoms in relatively light Zn–O–Sn bonds, whereas retaining the O atoms in Sn–O–Sn bonds, which have the heaviest equivalent mass for metal–oxygen bonds in the structure and have the smallest effect on IR transmission of the materials.[32,33] Meanwhile, the hetero-anionic $[SnOS_3]$ tetrahedra may exhibit large polarization, which will favor the material to generate a large SHG response.[25] By doing these, we have successfully synthesized the first hetero-anionic thiostannate, $Sr_2ZnSn_2OS_6$. It exhibits not only a wide IR transmission, but also a large SHG response, ∼0.7× $AgGaS_2$, which is two orders of magnitude larger than that of maternal $Sr_2ZnSi_2O_7$. These results indicate that $Sr_2ZnSn_2OS_6$ is a promising IR NLO crystal. Herein, we will report its synthesis, structure, and NLO properties.

Results and discussion

The polycrystalline sample of $Sr_2ZnSn_2OS_6$ was obtained by a solid-state reaction in a sealed silica tube (for more details see the ESI†). The purity of the sample was confirmed by powder X-ray diffraction (PXRD). In order to investigate the thermal behavior of $Sr_2ZnSn_2OS_6$, we carried out a series solid state reactions with different calcination temperatures and performed their powder XRD from 500 to 800 °C (Fig. S1†). It is clear that $Sr_2ZnSn_2OS_6$ is thermally stable until 750 °C. After 750 °C, $Sr_2ZnSn_2OS_6$ decomposes into SrS, SnS and ZnS (Fig. S1†). The millimeter-size crystal of $Sr_2ZnSn_2OS_6$ was grown by the solution method with SrS as the flux (Fig. S2†), and the specific crystal photograph is shown in Fig. S3.† The structure was determined by single crystal XRD and the crystallographic data are given in Table S1.†

$Sr_2ZnSn_2OS_6$ crystallizes in the NCS tetragonal space group $P\bar{4}2_1m$. In the asymmetric unit of $Sr_2ZnSn_2OS_6$, there are one unique Sr, one Zn, one Sn, one O and two S atom(s). Among them, the Sn atom is coordinated by one O atom and three S atoms to form the $SnOS_3$ tetrahedron with the distance of d(Sn–O) = 2.029(4) Å and Sn–S distances in the range of 2.321(2)–2.366(16) Å, respectively. The Zn atom is coordinated with four S atoms forming the typical ZnS_4 tetrahedron with identical Zn–S distance, d(Zn–S) = 2.333(16) Å (Fig. 1a). In the structures, three $SnOS_3$ tetrahedra and two ZnS_4 tetrahedra are connected to form an interesting pentagon ring (Fig. 1c). In the pentagon ring, the $SnOS_3$ tetrahedron connects with a ZnS_4 tetrahedron by sharing the S atoms, and the two $SnOS_3$ tetrahedra are connected by sharing the O atoms. These pentagons further form two-dimensional (2D) $[ZnSn_2OS_6]_\infty$ layers (Fig. 1b), which are separated by Sr^{2+} cations to form the structure of $Sr_2ZnSn_2OS_6$ (Fig. 1d). Regarding the Sr^{2+} cations, they are located in an eight-coordinated $SrOS_7$ bicapped trigonal prism with the d(Sr–O) = 2.788(5) Å and d(Sr–S) = 3.113(2)–3.150(17) Å, respectively (Table S2†). These bond distances are comparable to those of other reported compounds.[21] Bond valence calculations show that the bond valence sums (BVSs) for each atom are 2.12, 2.00, 4.04, and 1.73 for Sr^{2+}, Zn^{2+}, Sn^{4+}, and O^{2-}, respectively. The

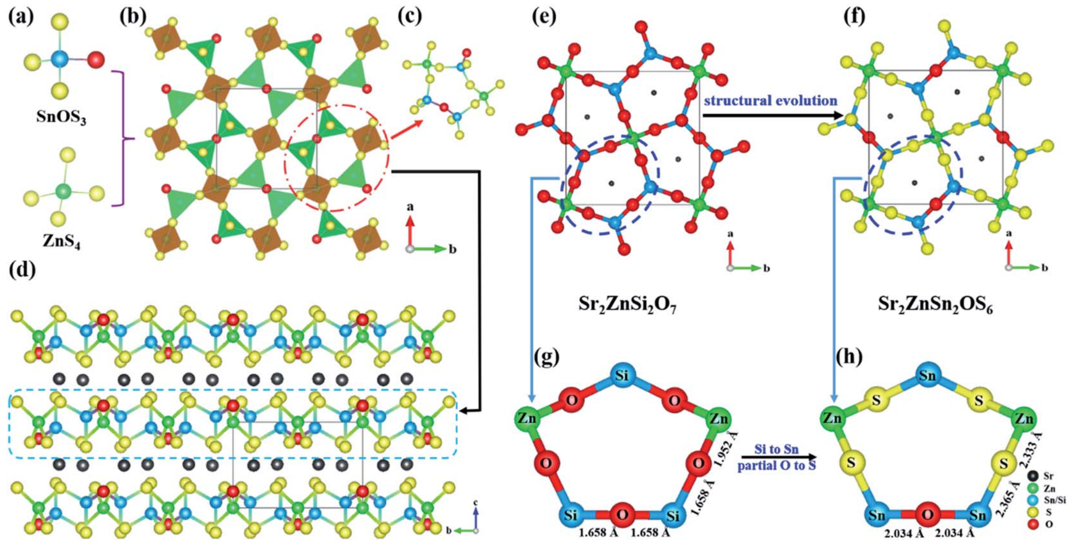

Fig. 1 (a) $[SnOS_3]$ and $[ZnS_4]$ tetrahedra. (b) The 2-dimensional $[ZnSn_2OS_6]^{4-}$ layers composed of pentagons. (c) The pentagonal ring composed of $[SnOS_3]$ and $[ZnS_4]$ tetrahedra. (d) The crystal structure of $Sr_2ZnSn_2OS_6$. (e and f) Structural evolution from $Sr_2ZnSi_2O_7$ to $Sr_2ZnSn_2OS_6$. (g) The pentagon consisting of Zn–O–Si and Si–O–Si bonds. (h) The pentagon consisting of Zn–S–Sn and Sn–O–Sn bonds.

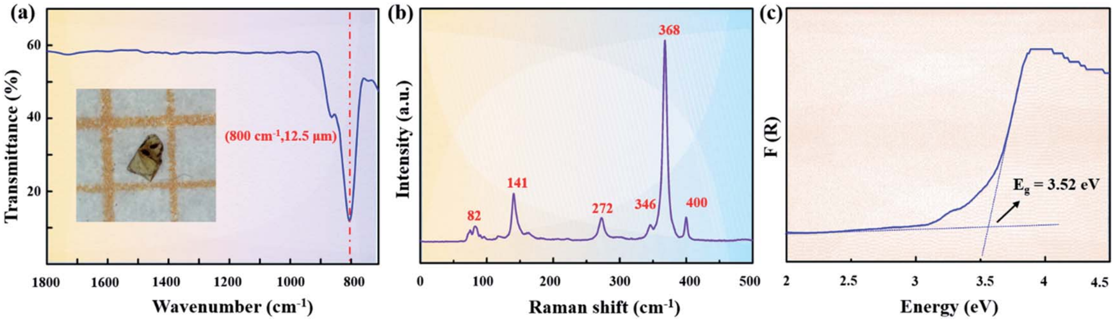

Fig. 2 (a) IR transmission spectrum from single crystals, (b) Raman spectrum, and (c) UV-vis-NIR diffuse reflectance spectrum of $Sr_2ZnSn_2OS_6$.

BVSs of S^{2-} anions are in the range of 2.08–2.14 (Table S3†). All the BVSs are consistent with the expected valences.

Structurally, $Sr_2ZnSn_2OS_6$ can be seen as a homologue of $Sr_2ZnSi_2O_7$ (Fig. 1e–h). Compared with $Sr_2ZnSi_2O_7$, $Sr_2ZnSn_2OS_6$ exhibits the following structural features: (i) the Si^{4+} cations in $Sr_2ZnSi_2O_7$ were substituted by the heavier Sn^{4+} cations, which are the heaviest cations but have similar coordination to Si^{4+} in group IV; (ii) all the terminal O atoms in the Zn–O or Sn–O bonds, and all the bridging O atoms in the Zn–O–Sn bonds are substituted by the heavier S atoms, while the O atoms in the Sn–O–Sn bonds are retained (Fig. 1e and f). The above substitution will be favorable for $Sr_2ZnSn_2OS_6$ to exhibit wide IR transmission. Generally, the IR absorption of materials mainly originates from the vibration of the groups. Thus, in $Sr_2ZnSn_2OS_6$, the large equivalent mass of $SnOS_3$ and ZnS_4 groups will be favorable for widening the IR transmission of materials. In $Sr_2ZnSi_2O_7$, the Si–O bonds have the lightest equivalent mass, so they have the greatest effect on IR transmission. Using the heavier Sn^{4+} cations to substitute Si^{4+} can reduce the effect. As shown in Fig. S4,† the peaks at 1123, 963, 894, and 832 cm^{-1} correspond to the asymmetric and symmetric stretching vibrations of Si–O bonds. The peak at 587 cm^{-1} can be assigned to the bending vibrations of Si–O bonds in $Sr_2ZnSi_2O_7$. Furthermore, a micron sized crystal was used to measure the IR transmission spectrum of $Sr_2ZnSn_2OS_6$. Similar measurements have also been found in the previous research.[34–37] It is clear that there is no obvious absorption in the range from 1800 to 800 cm^{-1}, corresponding to 5.5 to 12.5 μm (Fig. 2a). The absorption peak at 800 cm^{-1} can be assigned to the stretching vibration of the Sn–O–Sn bond.[38] In addition, except for the Si^{4+} cations, the terminal O atoms and bridging O atoms in those bonds with low equivalent mass (*e.g.* the O in the Zn–O–Sn bonds) are also more prone to vibrate than the bridging O atoms in the heavy Sn–O–Sn bonds. Therefore, substituting them with the relatively heavy S atoms would also be helpful to further widen the IR transmission region of the material. The rational substitution from $Sr_2ZnSi_2O_7$ to $Sr_2ZnSn_2OS_6$ can be attributed to the minimum distortion of pentagonal rings. In $Sr_2ZnSi_2O_7$, the pentagonal ring is composed of four long Si–O–Zn bonds and one short Si–O–Si bond (Fig. 1g). From $Sr_2ZnSi_2O_7$ to $Sr_2ZnSn_2OS_6$, substituting O atoms with S atoms in Sn–O–Zn bonds and retaining O atoms in the Sn–O–Sn bonds can best retain a similar pentagonal-ring-configuration, *i.e.* also including four long Sn–S–Zn bonds and one short Sn–O–Sn bond (Fig. 1h).

Furthermore, Raman spectroscopy of $Sr_2ZnSn_2OS_6$ is shown in Fig. 2b. In the Raman spectra, the absorption peaks at 400, 368, and 346 cm^{-1} can be attributed to the characteristic absorption of Sn–S modes, the peaks around 272 cm^{-1} should be from the Zn–S bonds and the absorption peaks below 200 cm^{-1} (including 141 and 82 cm^{-1}) are mainly attributed to Sr–S vibrations.[39–41]

The UV-vis-NIR diffuse reflectance spectrum in the range of 200–2500 nm was also measured by using a Shimadzu SolidSpec-3700DUV spectrophotometer (Fig. 2c). It was transformed into an *F*(*R*) *versus* (*hν*) curve based on the Kubelka–Munk function.[42] Extrapolating the linear part of the rising curve to zero, an experimental band gap of 3.52 eV can be obtained. The band gap of $Sr_2ZnSn_2OS_6$ is much larger than those in commercial $AgGaS_2$ (2.56 eV)[11] and $AgGaSe_2$ (1.83 eV).[12] Since the large bandgap will reduce the proportion of two photon or multiphoton absorption, the large band-gap is generally helpful for producing a large LDT.[43] So, the LDT of $Sr_2ZnSn_2OS_6$ was also measured by using a Q-switched pulse laser (1064 nm, 10 ns, 10 Hz) with a powder $AgGaS_2$ sample as the reference. It indicates that $Sr_2ZnSn_2OS_6$ has a good laser damage resistance, and the measured LDT (131 MW cm^{-2}) is about 10 times that of $AgGaS_2$ (12 MW cm^{-2}).[44]

$Sr_2ZnSn_2OS_6$ crystallizes in the NCS space group $P\bar{4}2_1m$. Its SHG response was measured based on the Kurtz–Perry method by using a laser with a wavelength of 2.09 μm and with powder $AgGaS_2$ as the reference.[45] The sample of $AgGaS_2$ was purchased

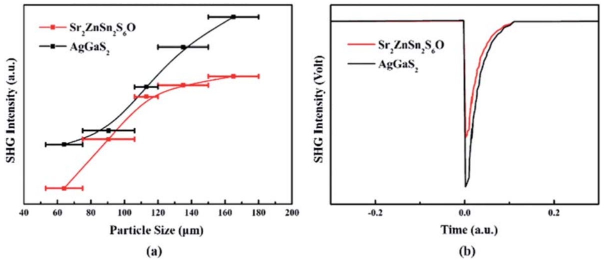

Fig. 3 (a) SHG intensity *versus* particle size for $Sr_2ZnSn_2OS_6$ and $AgGaS_2$. (b) Comparison of SHG intensities for $Sr_2ZnSn_2OS_6$ and $AgGaS_2$ at the particle sizes of 150–180 μm.

from Sichuan Ninth Research Institute (Fig. S5†) and the powder $AgGaS_2$ sample was obtained by grinding the $AgGaS_2$ crystal. As shown in Fig. 3a, the SHG intensities of $Sr_2ZnSn_2OS_6$ increase with its particle size. So, $Sr_2ZnSn_2OS_6$ can achieve type-I phase-matching. The SHG response with the particle size in the range of 150–180 μm is approximately 0.7× $AgGaS_2$ (Fig. 3b), indicating that $Sr_2ZnSn_2OS_6$ exhibits moderate SHG response. Apart from the large SHG response, a suitable birefringence is also necessary for the application of NLO crystals. Hence, we measured the birefringence of $Sr_2ZnSn_2OS_6$ by using a cross-polarizing microscope. The orientation of such a utilized crystal was determined as [100] by using the "Index Crystal Faces" program in Bruker SMART APEX III. The observed color of $Sr_2ZnSn_2OS_6$ in cross-polarized light is second-order yellow. The thickness of the crystal used for the measurement is 8 μm (Fig. S6†). According to the Michel-Levy chart, the retardation (*R* value) is 920 nm. Thus, the birefringence of $Sr_2ZnSn_2OS_6$ in the visible region is 0.12, which is large enough for ensuring the phase matching of $Sr_2ZnSn_2OS_6$.

The above measurements indicate that $Sr_2ZnSn_2OS_6$ not only exhibits well-balanced NLO properties, including a wide transmission region, large band-gap, and high LDT as well as moderate birefringence and SHG response (Fig. 4a), but also presents the first Sn-containing oxychalcogenide IR NLO with $[SnOS_3]$ hetero-anionic tetrahedra (Fig. 4b).[46–52] In order to better understand the origin of these excellent NLO properties, especially the moderate SHG response and birefringence, we further calculated the electronic structure of $Sr_2ZnSn_2OS_6$ through the first-principles calculation.

As shown in Fig. 5a, $Sr_2ZnSn_2OS_6$ is a direct-gap compound and the calculated band gap is 2.71 eV, which is smaller than the experimental value (3.52 eV). The smaller calculated band gap can be attributed to the limitation of the density functional theory (DFT) method.[53] The density of states (DOS) and partial densities of states (PDOS) of $Sr_2ZnSn_2OS_6$ are shown in Fig. 5b. The top of the valence band (VB) is predominately composed of O 2p and S 3p states, mixed with small amounts of Sn 5p, while the bottom of the conductive band (CB) mainly originates from O 2p, S 3p, and Sn 5s,5p states. As we know, the optical properties of a material are mainly affected by the electronic transitions between the energy levels close to the forbidden band. So, the SHG response and birefringence will be mainly determined by $[SnOS_3]$ and $[ZnS_4]$ tetrahedra (Fig. S7†). Particularly for $[SnOS_3]$ tetrahedra, owing to the part substitution of O and S, the dipole moment of the $SnOS_3$ tetrahedron is obviously larger than that of ZnS_4 (Table S5†). It indicates that $SnOS_3$ tetrahedra

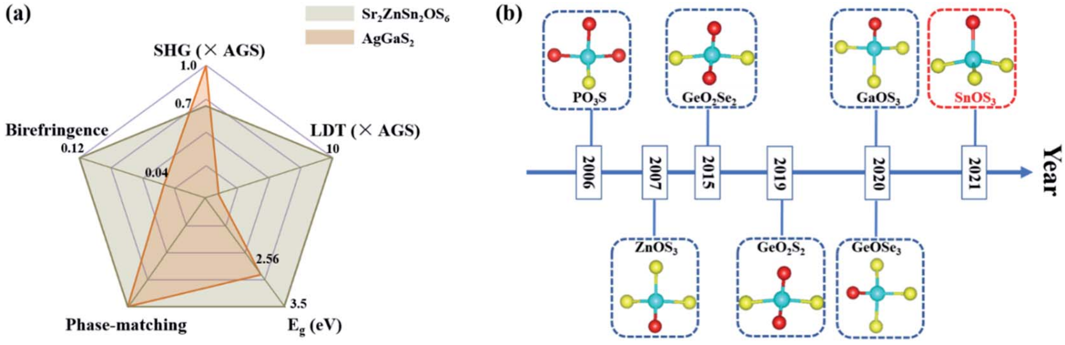

Fig. 4 (a) The excellent overall NLO performances of $Sr_2ZnSn_2OS_6$. (b) Timeline of the hetero-anionic NLO-active unit discovered in oxychalcogenides.

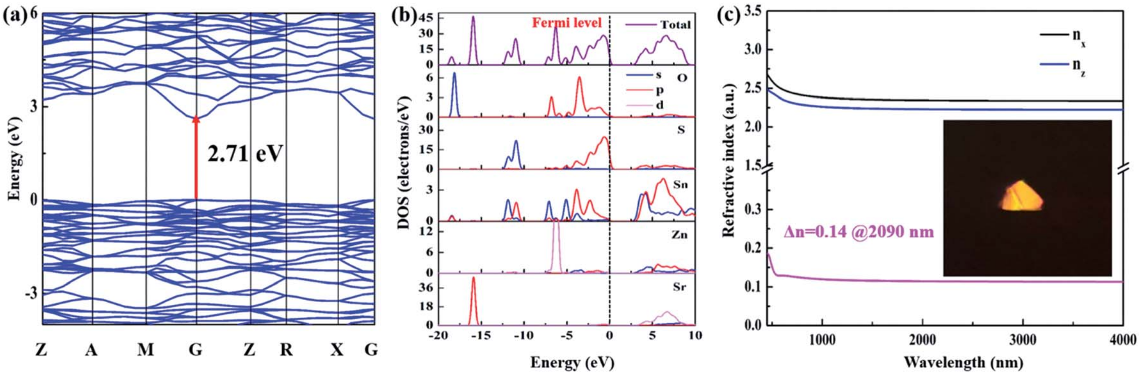

Fig. 5 (a) Calculated band structures of $Sr_2ZnSn_2OS_6$. (b) PDOS and TDOS plot of $Sr_2ZnSn_2OS_6$. (c) The calculated refractive dispersion curve of $Sr_2ZnSn_2OS_6$ (the inset image shows the crystal for the birefringence determination).

Table 1 Comparison of properties between $Sr_2ZnSn_2S_6O$ and other NLO oxychalcogenides[a]

Crystals	Space group	IR absorption edge (μm)	E_g (eV)	SHG (×AGS)	PM/NPM
$Sr_2ZnSn_2OS_6$	$P\bar{4}2_1m$	12.5	3.52	0.7	PM
$Sr_6Cd_2Sb_6O_7S_{10}$	Cm	15.5	1.89	4	PM
$SrZn_2OS_2$	$Pmn2_1$	—	3.86	0.06	PM
$Sr_3Ge_2O_4Se_3$	$R3m$	—	2.96	0.8	PM
$BaGeOSe_2$	$P2_12_12_1$	13.3	3.2	1.1	PM
$SrGeOSe_2$	$P2_12_12_1$	12.6	3.16	1.3	PM
$BaGeOS_2$	$P2_12_12_1$	—	4.1	0.5	NPM
$SrGeOS_2$	$P2_12_12_1$	—	3.9	0.4	NPM
$Sr_5Ga_8O_3S_{14}$	$P2_12_12$	13.4	3.9	0.8	NPM

[a] PM = phase matchability, NPM = non-phase matchability.

have the main contribution to the SHG response and birefringence of $Sr_2ZnSn_2OS_6$. Meanwhile, the dipole moments of ZnO_4 and SiO_4 in $Sr_2ZnSi_2O_7$ are also calculated (Fig. S8†). By comparing the dipole moments of SiO_4 (6.29 D) and $SnOS_3$ (6.77 D), it can be found that the mixed-anion $SnOS_3$ units can exhibit larger polarity in the structure. These results indicate that the rational substitutions of S for O and Sn for Si have contributed the enhancement of the NLO response in $Sr_2ZnSn_2OS_6$.

Based on the calculated electronic structure, the NLO coefficient and birefringence of $Sr_2ZnSn_2OS_6$ can also be calculated. $Sr_2ZnSn_2OS_6$ belongs to the point group of $\bar{4}2m$. It only has one non-zero independent SHG tensor, d_{14} under the restriction of Kleinman symmetry. The calculation shows $d_{14} = 4.48$ pm V^{-1}, which is comparable with the experimental results. Moreover, the refractive indices and birefringence (Δn) were also calculated. The calculated birefringence is shown in Fig. 5c, and the birefringence $\Delta n = 0.14$ at 2090 nm. These calculated results are also essentially consistent with the experimental ones.

Conclusions

In summary, based on the rational partial substitution of S^{2-} for O^{2-} anions in $Sr_2ZnSi_2O_7$, the first Sn-containing oxychalcogenide IR NLO crystal $Sr_2ZnSn_2OS_6$ has been successfully designed and synthesized. It can exhibit excellent NLO properties, including a wide IR transmission region, large band gap (3.52 eV), and high LDT (10× AGS) as well as a suitable SHG response (0.7× AGS) and birefringence (0.14 @ 2090 nm), which are comparable with other excellent oxychalcogenides (Table 1). These results show that $Sr_2ZnSn_2OS_6$ would be a promising IR NLO crystal. The excellent NLO properties of $Sr_2ZnSn_2OS_6$ can be attributed to the rational substitution of S^{2-} for O^{2-}, *i.e.* the terminal O atoms and the bridging O atoms in the light Zn–O–Sn bonds, which would lead to an insufficient IR transparency window, have been substituted by the heavier S, while the bridging O atoms in the heavy Sn–O–Sn bonds, which have a weak effect on the IR transparent region, are retained for constructing the distorted $SnOS_3$ groups to produce a moderate SHG response. These findings will be helpful to provide some new insights for the design of oxychalcogenide IR NLO crystals.

Data availability

Supporting data for this article is presented in the ESI.†

Author contributions

Conceptualization and supervision: H. W. Yu and H. P. Wu; synthesis and characterization (single-crystal XRD, powder XRD, IR, UV-vis-NIR and SHG measurements): Y. S. Cheng; all authors proof-read, provided comments, and approved the final version of this manuscript.

Conflicts of interest

There are no conflicts to declare.

Acknowledgements

This work is supported by the National Natural Science Foundation of China (Grant No. 22071179, 52172006, 51972230, 51890864, 61835014, 51890865) and Natural Science Foundation of Tianjin (Grant No. 21JCJQJC00090 and 20JCJQJC00060).

Notes and references

1 P. Becker, *Adv. Mater.*, 1998, **10**, 979–992.
2 R. E. Sykora, K. M. Ok, P. S. Halasyamani and T. E. Albrecht-Schmitt, *J. Am. Chem. Soc.*, 2002, **124**, 1951–1957.
3 H. Wu, S. Pan, K. R. Poeppelmeier, H. Li, D. Jia, Z. Chen, X. Fan, Y. Yang, J. M. Rondinelli and H. Luo, *J. Am. Chem. Soc.*, 2011, **133**, 7786–7790.
4 X. Wang, Y. Wang, B. Zhang, F. Zhang, Z. Yang and S. Pan, *Angew. Chem., Int. Ed.*, 2017, **56**, 14119–14123.
5 B. Zhang, G. Shi, Z. Yang, F. Zhang and S. Pan, *Angew. Chem., Int. Ed.*, 2017, **56**, 3916–3919.
6 C. T. Chen, B. C. Wu, A. D. Jiang and G. M. You, *Sci. China, Ser. B: Chem.*, 1985, **28**, 235–243.
7 C. T. Chen, Y. C. Wu, A. D. Jiang, B. C. Wu, G. M. You, R. K. Li and S. J. Lin, *J. Opt. Soc. Am. B*, 1989, **6**, 616–621.
8 G. Ryu, C. S. Yoon, T. P. J. Han and H. G. Gallagher, *J. Cryst. Growth*, 1998, **191**, 492–500.

9 H. Siegfried, *Z. Kristallogr.–Cryst. Mater.*, 1964, **120**, 401–414.

10 J. D. Bierlein and H. Vanherzeele, *J. Opt. Soc. Am. B*, 1989, **6**, 622–633.

11 A. O. Okorogu, S. B. Mirov, W. Lee, D. I. Crouthamel, N. Jenkins, A. Y. Dergachev, K. L. Vodopyanov and V. V. Badikov, *Opt. Commun.*, 1998, **155**, 307–312.

12 G. Boyd, H. Kasper, J. McFee and F. Storz, *IEEE J. Quantum Electron.*, 1972, **8**, 900–908.

13 G. D. Boyd, E. Buehler and F. G. Storz, *Appl. Phys. Lett.*, 1971, **18**, 301–304.

14 K. Wu, B. Zhang, Z. Yang and S. Pan, *J. Am. Chem. Soc.*, 2017, **139**, 14885–14888.

15 H. Chen, Y. Y. Li, B. X. Li, P. F. Liu, H. Lin, Q. L. Zhu and X. T. Wu, *Chem. Mater.*, 2020, **32**, 8012–8019.

16 B. B. Zhang, G. Q. Shi, Z. H. Yang, F. F. Zhang and S. L. Pan, *Angew. Chem., Int. Ed.*, 2017, **56**, 3916–3919.

17 J. Lu, J. N. Yue, L. Xiong, W. K. Zhang, L. Chen and L. M. Wu, *J. Am. Chem. Soc.*, 2019, **141**, 8093–8097.

18 G. H. Zou, N. Ye, L. Huang and X. S. Lin, *J. Am. Chem. Soc.*, 2011, **133**, 20001–20007.

19 Y. Wang, B. Zhang, Z. Yang and S. Pan, *Angew. Chem., Int. Ed.*, 2018, **57**, 2150–2154.

20 H. Yu, H. Wu, S. Pan, Z. Yang, X. Su and F. Zhang, *J. Mater. Chem.*, 2012, **22**, 9665–9670.

21 L. Kang, M. Zhou, J. Yao, Z. Lin, Y. Wu and C. Chen, *J. Am. Chem. Soc.*, 2015, **137**, 13049–13059.

22 H. Yu, W. Zhang and P. S. Halasyamani, *Cryst. Growth Des.*, 2016, **16**, 1081–1087.

23 G. Han, Y. Wang, X. Su, Z. Yang and S. Pan, *Sci. Rep.*, 2017, **7**, 1901.

24 Y. Tsujimoto, C. A. Juillerat, W. Zhang, K. Fujii, M. Yashima, P. S. Halasyamani and H.-C. zur Loye, *Chem. Mater.*, 2018, **30**, 6486–6493.

25 R. Wang, Y. Guo, X. Zhang, Y. Xiao, J. Yao and F. Huang, *Inorg. Chem.*, 2020, **59**, 9944–9950.

26 M. Y. Ran, Z. Ma, H. Chen, B. Li, X. T. Wu, H. Lin and Q. L. Zhu, *Chem. Mater.*, 2020, **32**, 5890–5896.

27 B. W. Liu, X. M. Jiang, G. E. Wang, H. Y. Zeng, M. J. Zhang, S. F. Li, W. H. Guo and G. C. Guo, *Chem. Mater.*, 2015, **27**, 8189–8192.

28 R. Wang, F. Liang, F. Wang, Y. Guo, X. Zhang, Y. Xiao, K. Bu, Z. Lin, J. Yao, T. Zhai and F. Huang, *Angew. Chem., Int. Ed.*, 2019, **58**, 8078–8081.

29 M. Mutailipu, Z. Li, M. Zhang, D. Hou, Z. Yang, B. Zhang, H. Wu and S. Pan, *Phys. Chem. Chem. Phys.*, 2016, **18**, 32931–32936.

30 H. Yu, W. Zhang, J. Young, J. M. Rondinelli and P. S. Halasyamani, *J. Am. Chem. Soc.*, 2015, **138**, 88–91.

31 K. Chen, C. Lin, S. Zhang, G. Peng, Y. Chen, D. Zhao, H. Fan, S. Yang, X. Wen, M. Luo, Z. Lin and N. Ye, *Chem. Mater.*, 2021, **33**, 6012–6017.

32 X. Chen, Q. Jing and K. M. Ok, *Angew. Chem., Int. Ed.*, 2020, **59**, 20323–20327.

33 X. Luo, Z. Li, F. Liang, Y. Guo, Y. Wu, Z. Lin and J. Yao, *Inorg. Chem.*, 2019, **58**, 7118–7125.

34 W. Xing, F. Liang, C. Tang, E. Uykur, Z. Lin, J. Yao, W. Yin and B. Kang, *ACS Appl. Mater. Interfaces*, 2021, **13**, 37331–37338.

35 J. Chen, H. Chen, F. Xu, L. Cao, X. Jiang, S. Yang, Y. Sun, X. Zhao, C. Lin and N. Ye, *J. Am. Chem. Soc.*, 2021, **143**, 10309–10316.

36 Y. Hu, C. Wu, X. Jiang, Z. Wang, Z. Huang, Z. Lin, X. Long, M. G. Humphrey and C. Zhang, *J. Am. Chem. Soc.*, 2021, **143**, 12455–12459.

37 W. Xing, C. Tang, N. Wang, C. Li, E. Uykur, J. Wu, Z. Lin, J. Yao, W. Yin and B. Kang, *Adv. Opt. Mater.*, 2021, **9**, 2100563.

38 P. Pascuta, L. Pop, S. Rada, M. Bosca and E. Culea, *Vib. Spectrosc.*, 2008, **48**, 281–284.

39 J. He, Y. Guo, W. Huang, X. Zhang, J. Yao, T. Zhai and F. Huang, *Inorg. Chem.*, 2018, **57**, 9918–9924.

40 K. Wu, Z. Yang and S. Pan, *Angew. Chem., Int. Ed.*, 2016, **55**, 6713–6715.

41 X. Luo, Z. Li, F. Liang, Y. Guo, Y. Wu, Z. Lin and J. Yao, *Inorg. Chem.*, 2019, **58**, 7118–7125.

42 E. L. Simmons, *Appl. Opt.*, 1975, **14**, 1380–1386.

43 T. W. Walker, A. H. Guenther and P. Nielsen, *IEEE J. Quantum Electron.*, 1981, **17**, 2053–2065.

44 K. Wu, Z. Yang and S. Pan, *Chem. Mater.*, 2016, **28**, 2795–2801.

45 S. K. Kurtz and T. T. Perry, *J. Appl. Phys.*, 1968, **39**, 3798–3813.

46 X. Luo, F. Liang, M. Zhou, Y. Guo, Z. Li, Z. Lin, J. Yao and Y. Wu, *Inorg. Chem.*, 2018, **57**, 9446–9452.

47 P. A. Maggard, T. S. Nault, C. L. Stern and K. R. Poeppelmeier, *Solid State Chem.*, 2003, **175**, 27–33.

48 J. Zhang, Z. Zhang, W. Zhang, Q. Zheng, Y. Sun, C. Zhang and X. Tao, *Chem. Mater.*, 2011, **23**, 3752–3761.

49 W. Xing, P. Fang, N. Wang, Z. Li, Z. Lin, J. Yao, W. Yin and B. Kang, *Inorg. Chem.*, 2020, **59**, 16716–16724.

50 H. Yan, Y. Matsushita, K. Yamaura and Y. Tsujimoto, *Angew. Chem., Int. Ed.*, 2021, **60**, 26561–26565.

51 Y. F. Shi, W. B. Wei, X. T. Wu, H. Lin and Q. L. Zhu, *Dalton Trans.*, 2021, **50**, 4112–4118.

52 X. Zhang, Y. Xiao, R. Wang, P. Fu, C. Zheng and F. Huang, *Dalton Trans.*, 2019, **48**, 14662–14668.

53 R. W. Godby, M. Schlter and L. J. Sham, *Phys. Rev. B: Condens. Matter Mater. Phys.*, 1987, **36**, 6497–6650.